Postprint of: Żak A., Krawczuk M.: A higher order transversely deformable shell-type spectral finite element for dynamic analysis of isotropic structures. FINITE ELEMENTS IN ANALYSIS AND DESIGN. Vol. 142, (2018), p. 17-29. DOI: 10.1016/j.finel.2017.12.007

A higher order transversely deformable shell-type spectral finite element for dynamic analysis of isotropic structures

A. Żak*, M. Krawczuk

Gdansk University of Technology, Faculty of Electrical and Control Engineering, ul. Narutowicza 11/12, 80-234 Gdansk, Poland

Abstract

This paper deals with certain aspects related to the dynamic behaviour of isotropic shell-like structures analysed by the use of a higher order transversely deformable shell-type spectral finite element newly formulated and the approach known as the Time-domain Spectral Finite Element Method (TD-SFEM). Although recently this spectral approach is reported in the literature as a very powerful numerical tool used to solve various wave propagation problems, its properties make it also very well suited to solve static and dynamic modal problems. The robustness and effectiveness of the current spectral approach has been successfully demonstrated by the authors in the case of thin-walled spherical shell structures through a series of numerical tests comprising the analysis of natural frequencies and modes of vibration of an isotropic spherical shell as well as the wave propagation analysis in the case of the same spherical shell and a half-pipe shell-like structure.

Keywords: higher order shell theory; transverse deformation; spectral finite element method; modal analysis; elastic wave propagation

1. Introduction

Investigation, modelling and analysis of wave propagation in shell-like structures have been the subject of scientific interest for many years [1–3]. As a result, during that time various continuous [4–8] and discrete models [9–11] were developed and tested by many authors.

However, the main problem related to continuous models is that they are usually restricted to structures of simple geometries and boundary conditions, as well as homogeneous material properties. In contrast, discrete models can be easily employed to investigate structures of complex geometries and boundary conditions or material properties. Nevertheless, discrete models, in the case of wave propagation problems, need proper spatial discretisation. Among many discrete methods, which are often applied for wave propagation modelling and analysis, the Spectral Finite Element Method (SFEM) appears as an effective and powerful tool [12]. However, it should be remembered that two different spectral approaches exist in the literature. The first is called the Frequency-domain Spectral Finite Element Method (FD-SFEM) and was originally proposed by Doyle [13, 14] and later developed by Gopalakrishnan [15, 16]. The second approach, proposed by Patera [17], is called the Time-domain Spectral Element Method (TD-SFEM). In the case of two-dimensional (2-D) or three-dimensional problems (3-D) the time-domain formulation of SFEM is much more effective than the frequency-domain formulation of the method.

In fact TD-SFEM is very similar to the well-known Finite Element Method (FEM). The main difference between them comes from the fact that TD-SFEM employs elemental shape functions based on Lobatto or Chebyshev approximation polynomials with elemental nodes located at points, which are the roots of these

*Corresponding author

Email addresses: arkadiusz.zak@pg.gda.pl (A. Żak), marek.krawczuk@pg.gda.pl (M. Krawczuk)

polynomials. As a consequence the nodes are not equidistant. Additionally, thanks to the orthogonality of the approximation polynomials elemental inertia matrices are diagonal in the case of Lobatto polynomials, or almost diagonal in the case of Chebyshev polynomials. Such forms of elemental inertia matrices allow for the application of more effective and accurate as well as less time consuming techniques to integrate the equations of motion.

In this paper a new multi-mode formulation of a higher order transversely deformable shell-type spectral finite element (SFE) for dynamic analysis of isotropic structures is presented and analysed. The accuracy of the formulation proposed is assessed by comparison of dispersion curves obtained for the current model with dispersion curves obtained for exact solutions of the problem as well as comparison with shell theories well-known from the literature.

Finally, in order to demonstrate the effectiveness of the current formulation of a higher order transversely deformable shell-type SFE a series of numerical tests were performed. These comprised the analysis of natural frequencies and modes of vibration of an isotropic spherical shell as well as the wave propagation analysis in the case of the same spherical shell and a half-pipe shell-like structure. Thanks to this, appropriate conclusions were formulated as a general guidance for the application of the current element and solution techniques in the case of various dynamic problems.

2. Shell element formulation

2.1. Displacement field

In comparison to classical shell theories the current formulation of a higher order transversely deformable shell-type SFE takes advantage of an extended form of the displacement field. According to this formulation the element has six degrees of freedom and takes into account the transverse deformation of the element. This feature of the element becomes very important, when high frequency dynamic responses are to be studied [11]. The shell element under investigation is presented in Fig. 1.

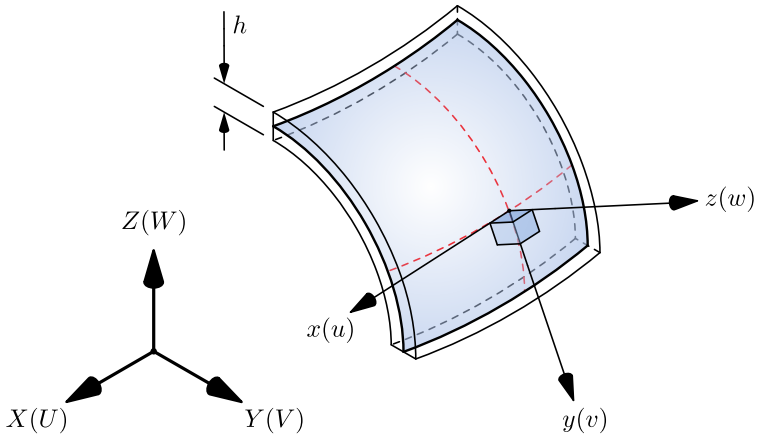

Figure 1: A shell SFE in the local xyz and global XYZ coordinate systems.

Additional displacement terms of the element displacement field represent higher-order terms of the field expansion into the Maclaurin series. They can be evaluated thanks to the application of the zero-traction boundary conditions for τ_{yz}, τ_{zx} as well as σ_{zz} stress components on the lower and upper surfaces of the element [1–3], in a similar manner as shown in [18]. Following the same approach as used in [19, 20] the displacement field of the current shell element may be represented, in the local coordinate system of the element xyz, as:

$$\begin{array}{rcccccccc} u & = & \phi_0 & + & a\zeta\phi_1 & + & (1-\zeta^2)\phi_2 & + & a\zeta(1-\zeta^2)\phi_3 \\ v & = & \psi_0 & + & a\zeta\psi_1 & + & (1-\zeta^2)\psi_2 & + & a\zeta(1-\zeta^2)\psi_3 \\ w & = & \theta_0 & + & a\zeta\theta_1 & + & (1-\zeta^2)\theta_2 & + & a\zeta(1-\zeta^2)\theta_3 \end{array} \tag{1}$$

where symbols ζ and a are defined by relations $z = a\zeta$ and $h = 2a$, while h is the thickness of the element.

It should be noted that the displacement components $\phi_i(i = 0, \ldots, 3)$, $\psi_i(i = 0, \ldots, 3)$ and $\theta_i(i = 0, \ldots, 3)$, remain certain unknown functions of the spatial coordinates x and y defined at the mid-plane of the element. They can be associated with either symmetric (*membrane*) or anti-symmetric (*bending*) behaviour of the element. In the case of the symmetric (*membrane*) behaviour these are the in-plane displacement functions $\phi_i(i = 0, 2)$ and $\psi_i(i = 0, 2)$ as well as the transverse displacement functions $\theta_i(i = 1, 3)$. On the other hand the anti-symmetric (*bending*) behaviour is associated with the remaining in-plane displacement functions $\phi_i(i = 1, 3)$ and $\psi_i(i = 1, 3)$ as well as the transverse displacement functions $\theta_i(i = 0, 2)$.

As mentioned earlier the application of the zero-traction boundary conditions for τ_{yz}, τ_{zx} as well as σ_{zz} stress components on the upper and lower surfaces of the element enables one to reduce the total number of unknown functions (element degrees of freedom) from eight to six. This leads to certain relations for the higher-order terms $\phi_i(i = 2, 3)$, $\psi_i(i = 2, 3)$ and $\theta_i(i = 2, 3)$, which can be expressed as dependent on the remaining lower order terms $\phi_i(i = 0, 1)$, $\psi_i(i = 0, 1)$ and $\theta_i(i = 0, 1)$ for the symmetric and anti-symmetric displacement components:

- for symmetric (*membrane*) behaviour:

$$\begin{aligned} 2\phi_2 &= a^2 \partial_x \theta_1 \\ 2\psi_2 &= a^2 \partial_y \theta_1 \\ 2\theta_3 &= \theta_1 + \tfrac{\lambda}{\lambda+2\mu}(\partial_x \phi_0 + \partial_y \psi_0) \end{aligned} \tag{2}$$

- for anti-symmetric (*bending*) behaviour:

$$\begin{aligned} 2\phi_3 &= \phi_1 + \partial_x \theta_0 \\ 2\psi_3 &= \psi_1 + \partial_y \theta_0 \\ 2\theta_2 &= a^2 \tfrac{\lambda}{\lambda+2\mu}(\partial_x \phi_1 + \partial_y \psi_1) \end{aligned} \tag{3}$$

where λ and μ are the Lamé constants.

Taking into account the relations given by Eqs. (2) and Eqs. (3) the strain field associated with the current definition of the displacement field can be easily defined. Based on that definition the characteristic elemental inertia $[\boldsymbol{M}]$ and stiffness $[\boldsymbol{K}]$ matrices can be evaluated after assuming a certain polynomial order m as well as an approximation method (Lobatto of Chebyshev) for the unknown functions $\phi_i(i = 0, 1)$, $\psi_i(i = 0, 1)$ and $\theta_i(i = 0, 1)$. This common and standard procedure for the classical FEM approach as well as TD-SFEM is well described and presented in [21–23].

However, due to the fact that the higher order terms, given by Eqs. (2) and Eqs. (3), involve local derivatives of the unknown functions $\phi_i(i = 0, 1)$, $\psi_i(i = 0, 1)$ and $\theta_i(i = 0, 1)$, the evaluation process of the characteristic elemental inertia $[\boldsymbol{M}]$ and stiffness $[\boldsymbol{K}]$ matrices is presented with more details in the following *Section* 2.4 of this paper.

2.2. Dispersion curves

Dispersion relations or dispersion curves provide very important information about the dependence of the phase and group velocities c_p and c_g on the frequency f, or the wave number k, for elastic waves propagating within structures of interest. They also help to estimate signal propagation times or distances, which on the other hand is very important in all damage detection strategies that are based on the propagation of guided elastic waves [24–27]. Dispersion relations for thin isotropic plates were extensively studied in the past by many researchers, with the results of the fundamental analytical research on that subject presented in [28, 29]. Against these analytical relations all new theories developed should be assessed and verified in order to define their applicability range. This procedure was also used by the authors of this work.

Following the methodology described in [11] the dispersion curves for the phase c_p and group velocities c_g, related with the displacement field given by Eqs. (1), can be obtained in a relatively straightforward manner by the use of Hamilton's principle [14]. Under assumption of small strains and displacements, the virtual work $\mathbb{W}$ associated with the deformation and motion of the shell element under investigation, may be

expressed in terms of its strain energy $\mathbb{U}$, kinetic energy $\mathbb{T}$, as well as the work of external forces $\mathbb{F}$. Bearing in mind the relations given by Eqs. (2) and Eqs. (3) a set of coupled equations of motion can be obtained for the unknown functions $\phi_i (i = 0, 1)$, $\psi_i (i = 0, 1)$ and $\theta_i (i = 0, 1)$ that can be presented in the following form:

- for symmetric (*membrane*) behaviour:

$$\begin{aligned}
&L_1 s_1 - (c_l^2 - c_s^2)\partial_{xy} s_2 - (c_l^2 - 2c_s^2)\partial_x \theta_1 = 0 \\
&L_2 s_2 - (c_l^2 - c_s^2)\partial_{xy} s_1 - (c_l^2 - 2c_s^2)\partial_y \theta_1 = 0 \\
&L_3 s_3 + (c_l^2 - c_s^2)(\partial_x s_1 + \partial_y s_2) - c_s^2(\partial_x \phi_0 + \partial_y \psi_0) + c_l^2 \theta_1 = 0 \\
&s_1 = \phi_0 + \tfrac{2}{3}\phi_2 \\
&s_2 = \psi_0 + \tfrac{2}{3}\psi_2 \\
&s_3 = \tfrac{1}{3}a^2(\theta_1 + \tfrac{2}{5}\theta_3)
\end{aligned} \tag{4}$$

- for anti-symmetric (*bending*) behaviour:

$$\begin{aligned}
&L_1 s_4 - (c_l^2 - c_s^2)\partial_{xy} s_5 - \tfrac{2}{3}(c_l^2 - 2c_s^2)\partial_x \theta_2 - c_s^2 \phi_1 = 0 \\
&L_2 s_5 - (c_l^2 - c_s^2)\partial_{xy} s_4 - \tfrac{2}{3}(c_l^2 - 2c_s^2)\partial_y \theta_2 - c_s^2 \psi_1 = 0 \\
&L_3 s_6 - c_s^2(\partial_x \phi_1 + \partial_y \psi_1) = 0 \\
&s_4 = \tfrac{1}{3}a^2(\phi_1 + \tfrac{2}{5}\phi_3) \\
&s_5 = \tfrac{1}{3}a^2(\psi_1 + \tfrac{2}{5}\psi_3) \\
&s_6 = \theta_0 + \tfrac{2}{3}\theta_2
\end{aligned} \tag{5}$$

where $L_i (i = 1, \ldots, 3)$ are defined as follows:

$$\begin{aligned}
L_1 &\equiv \partial_{tt} - c_l^2 \partial_{xx} - c_s^2 \partial_{yy} \\
L_2 &\equiv \partial_{tt} - c_l^2 \partial_{yy} - c_s^2 \partial_{xx} \\
L_3 &\equiv \partial_{tt} - c_s^2 (\partial_{xx} + \partial_{yy})
\end{aligned} \tag{6}$$

and where $c_l^2 = (\lambda + 2\mu)/\rho$ and $c_s^2 = \mu/\rho$ denote the squares of velocities of the longitudinal and shear waves [14], respectively.

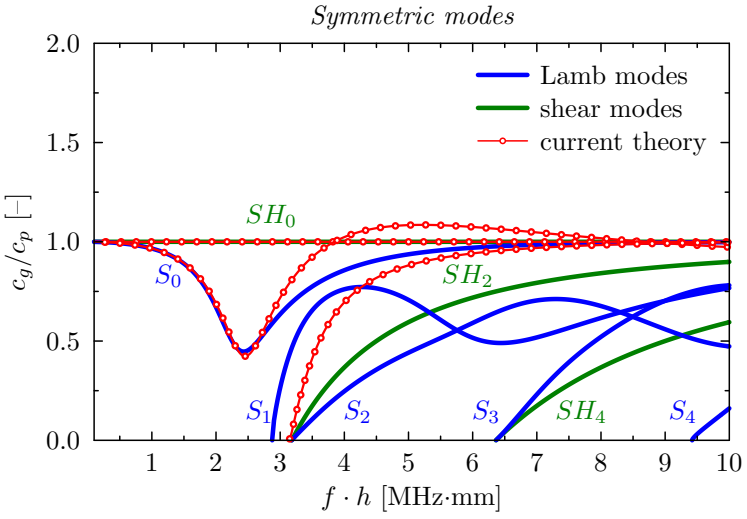

Figure 2: Dispersion curves for the velocity ratios c_g/c_p based on the current shell theory obtained for the symmetric (*membrane*) solutions ($c_l = 6.3$ km/s, $c_t = 3.2$ km/s).

In order to obtain dispersion curves for the phase c_p and group velocities c_g, associated with either symmetric (*membrane*) or anti-symmetric (*bending*) behaviour of the shell element, solutions of Eqs. (4) and

Eqs. (5) can be assumed as representing harmonic waves [2] for each independent displacement component $\phi_i(i=0,1)$, $\psi_i(i=0,1)$ and $\theta_i(i=0,1)$:

$$\begin{aligned}\phi_i &= \langle \boldsymbol{\phi}_i \rangle \exp[-j(k_x x + k_y y + \omega t)] \\ \psi_i &= \langle \boldsymbol{\psi}_i \rangle \exp[-j(k_x x + k_y y + \omega t)] \\ \theta_i &= \langle \boldsymbol{\theta}_i \rangle \exp[-j(k_x x + k_y y + \omega t)]\end{aligned} \tag{7}$$

where $\langle \boldsymbol{\phi}_i \rangle (i=0,1)$, $\langle \boldsymbol{\psi}_i \rangle (i=0,1)$ and $\langle \boldsymbol{\theta}_i \rangle (i=0,1)$ are the amplitudes of these harmonic waves, while k_x and k_y denote the wave numbers in x and y directions, ω is the angular frequency and $j = \sqrt{-1}$.

Two independent systems of linear homogeneous equations are obtained for the symmetric (*membrane*) and anti-symmetric (*bending*) behaviour by a simple substitution of Eqs. (7) into Eqs. (4) and Eqs. (5). These two systems can be solved only then when their determinants vanish, which leads to two independent characteristic equations associated with the problem. The roots of the characteristic equations define particular symmetric (*membrane*) and anti-symmetric (*bending*) wave propagation modes and link together the wave number $k^2 = k_x^2 + k_y^2$ with the angular frequency ω. In this way dispersion curves for changes in the phase c_p and group c_g velocities can be easily calculated and plotted, as presented in Fig. 2 and Fig. 3. In these cases results of numerical calculation were obtained for a thin aluminium layer ($E = 72.7$ GPa, $\nu = 0.33$, $\rho = 2700$ kg/m^3) and plotted as the velocity ratios c_g/c_p.

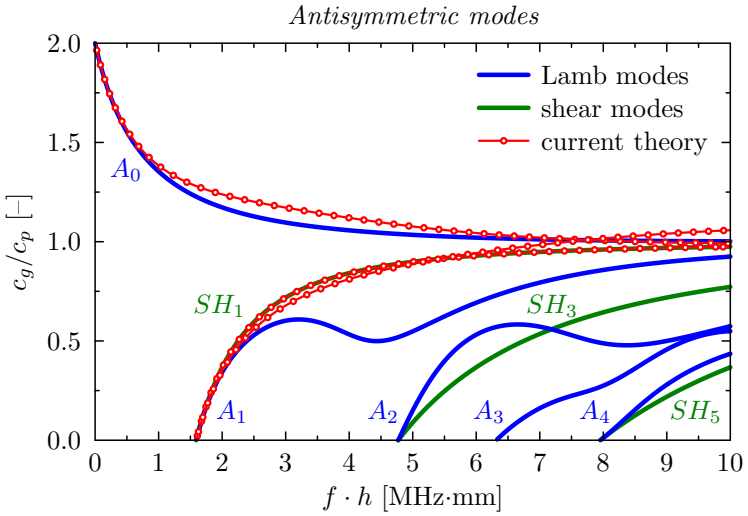

Figure 3: Dispersion curves for the velocity ratios c_g/c_p based on the current shell theory obtained for the anti-symmetric (*bending*) solutions ($c_l = 6.3$ km/s, $c_t = 3.2$ km/s).

Six dispersion curves, associated with the six independent displacement components $\phi_i(i=0,1)$, $\psi_i(i=0,1)$ and $\theta_i(i=0,1)$, can be easily distinguished based on Fig. 2 and Fig. 3. They represent symmetric (*membrane*) and anti-symmetric (*bending*) modes associated with the current formulation of the shell element. These are four modes corresponding to Lamb solutions: two symmetric modes S_0, S_1 and two anti-symmetric modes A_0, A_1, as well as two modes associated with horizontal symmetric SH_0 and anti-symmetric SH_1 shear waves. It should be emphasised here that the results presented in Fig. 2 and Fig. 3 confirm that the current formulation of the shell element, utilising the extended form of the displacement field, enables one to investigate propagation of elastic waves in shell-like structures associated with their either symmetric or anti-symmetric dynamic behaviour.

2.3. Approximation error

In general two kinds of errors play significant roles strongly influencing results of numerical simulations in the case of dynamic problems solved numerically. The first type of error is a discretisation error ϵ that comes from the fact that continuous structures, characterised by infinite numbers of degrees of freedom, are

typically represented by a certain number of discrete points thus reducing these infinite numbers to finite sets. This error becomes very important in the case of high frequency dynamic responses as well as wave propagation problems and can be reduced by increasing the size of numerical models.

The second type of error is a modelling error δ and it results from the fact that the dynamic behaviour of investigated structures is usually described by certain approximated theories that remain valid only in a range of applications. As in the case of the discretisation error ϵ the modelling error δ becomes very important at high frequency regimes and can be reduced by the application of higher order refined theories. It should be emphasised that these two kinds of errors are independent of each other. Thus decreasing the value of the discretisation error ϵ by increasing the number of model degrees of freedom has no effect on the value of the modelling error δ.

In the case of the higher order shell theory under consideration the modelling error δ was assessed based on the dispersion curves presented in Fig. 2 and Fig. 3. This error was calculated for the fundamental symmetric modes S_0 and SH_0 as well as the fundamental anti-symmetric A_0 and SH_1 modes. Its evaluation was based on the appropriate ratios c_g/c_p of the group velocity c_g and the phase velocity c_p as:

$$\delta = \frac{c_b - c_a}{c_a} \times 100\% \tag{8}$$

where c_b denotes the velocity ratio c_g/c_p obtained by the use of the current shell theory, while c_a refers to the velocity ratio c_g/c_p obtained from the analytical solutions.

At this point it is very interesting to note that the modelling error δ was equal to zero in the case of both fundamental symmetric and anti-symmetric shear modes SH_0 and SH_1 within the whole range of the frequency parameter $f \cdot h$ taken into account. For the fundamental symmetric (*membrane*) S_0 and anti-symmetric (*bending*) A_0 modes changes in the relative error δ are illustrated by Fig. 4 as a function of the frequency parameter $f \cdot h$.

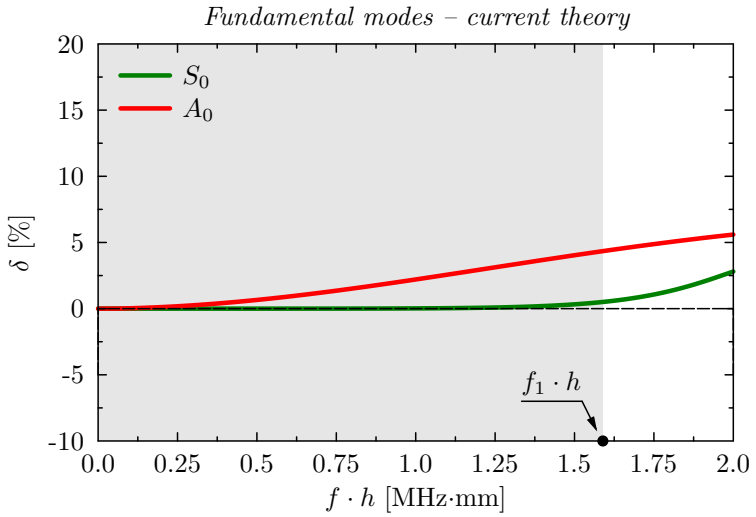

Figure 4: Relative error δ for the fundamental symmetric (*membrane*) and anti-symmetric (*bending*) modes based on the current shell theory measured against Lamb solutions ($c_l = 6.3$ km/s, $c_t = 3.2$ km/s).

It can be noted from Fig. 4 that the symmetric (*membrane*) S_0 mode is characterised by very small values of the modelling error δ up to the frequency parameter $f_1 \cdot h$ of 1.59 MHz·mm, corresponding to the first cut-off frequency f_1, i.e. the value of the frequency f at which the second wave propagation mode SH_1 appears. At this point the error δ reaches 0.5%. Also at this point two anti-symmetric modes start to propagate simultaneously as the A_1 and SH_1 modes, as presented in Fig. 3. From this moment on, the modelling error δ increases. In contrast, the modelling error δ calculated for the anti-symmetric (*bending*) A_0 mode stays moderate and positive. The modelling error δ reaches its maximum value of 4.4% for the first cut-off frequency f_1.

In order to compare the current shell theory with two other popular shell theories widely exploited in the literature, in a similar manner as before, the modelling errors δ associated with the Mindlin and Reddy shell theories were evaluated also for the fundamental symmetric (*membrane*) S_0 and anti-symmetric (*bending*) A_0 modes, as presented in Fig. 5 and Fig. 6. Since both the Mindlin and Reddy shell theories approximate the in-plane displacements in the same manner the modelling error related to the symmetric (*membrane*) S_0 mode exhibits the same type of behaviour. It can be seen that the error δ increases very rapidly with an increase in the frequency parameter $f \cdot h$. It reaches 15.5% for the frequency parameter $f_1 \cdot h$ of 1.59 MHz·mm, corresponding to the first cut-off frequency f_1.

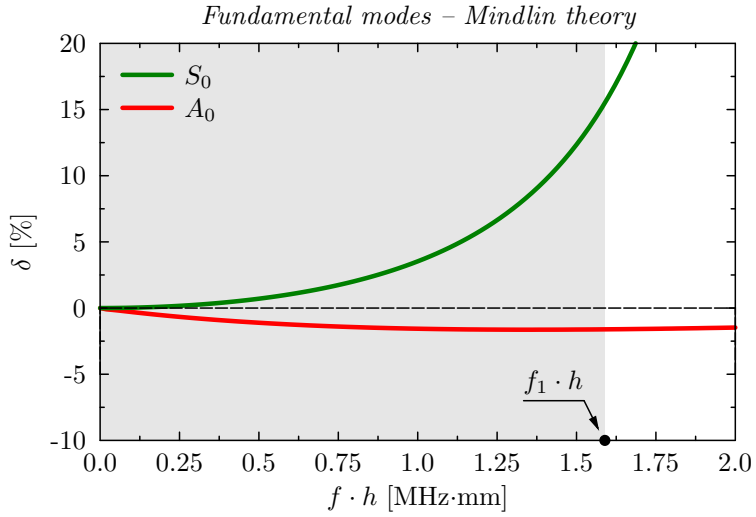

Figure 5: Relative error δ for the fundamental symmetric (*membrane*) and anti-symmetric (*bending*) modes based on the Mindlin shell theory measured against Lamb solutions ($c_l = 6.3$ km/s, $c_t = 3.2$ km/s).

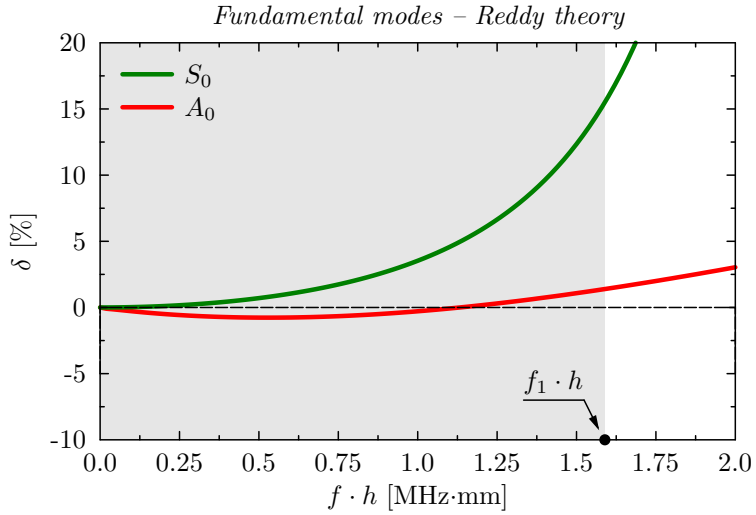

Figure 6: Relative error δ for the fundamental symmetric (*membrane*) and anti-symmetric (*bending*) modes based on the Reddy shell theory measured against Lamb solutions ($c_l = 6.3$ km/s, $c_t = 3.2$ km/s).

In the case of the fundamental anti-symmetric (*bending*) A_0 modes the observed behaviour is different for the Mindlin and Reddy shell theories. The modelling error δ associated with the Mindlin shell theory is relatively small in the whole range of the frequency parameter $f \cdot h$ under investigation. It takes its highest

negative value of -1.6% around the frequency parameter $f_1 \cdot h$ of 1.59 MHz·mm, corresponding to the first cut-off frequency f_1. In contrast, the modelling error δ associated with the Reddy shell theory takes its highest negative value of -0.8% around the frequency parameter $f_1 \cdot h$ of 0.5 MHz·mm to increase up to 1.4% around the frequency parameter $f_1 \cdot h$ of 1.59 MHz·mm corresponding to the first cut-off frequency f_1.

For better presentation of differences and similarities between the shell behaviour theories considered above Tab. 1 is given. It summarises particular shell theories in terms of wave propagation modes used by these theories as well as the form of displacement components $\phi_i (i = 0, \ldots, 3)$, $\psi_i (i = 0, \ldots, 3)$ and $\theta_i (i = 0, \ldots, 3)$. For completeness Tab. 1 also includes the Kirchhoff shell theory.

Table 1: Displacement field components and wave propagation modes available for selected shell theories: Kirchhoff, Mindlin, Reddy and a higher order transversely deformable shell theory developed by the authors.

Theory	Modes		Component	
Kirchhoff	S_0 A_0 SH_0	$\phi_0 \neq 0$ $\phi_1 = -\partial_x \theta_0$ $\phi_2 = 0$ $\phi_3 = 0$	$\psi_0 \neq 0$ $\psi_1 = -\partial_y \theta_0$ $\psi_2 = 0$ $\psi_3 = 0$	$\theta_0 \neq 0$ $\theta_1 = 0$ $\theta_2 = 0$ $\theta_3 = 0$
Mindlin	S_0 A_0,A_1 SH_0,SH_1	$\phi_0 \neq 0$ $\phi_1 \neq 0$ $\phi_2 = 0$ $\phi_3 = 0$	$\psi_0 \neq 0$ $\psi_1 \neq 0$ $\psi_2 = 0$ $\psi_3 = 0$	$\theta_0 \neq 0$ $\theta_1 = 0$ $\theta_2 = 0$ $\theta_3 = 0$
Reddy	S_0 A_0,A_1 SH_0,SH_1	$\phi_0 \neq 0$ $\phi_1 \neq 0$ $\phi_2 = 0$ $2\phi_3 = \phi_1 + \partial_x \theta_0$	$\psi_0 \neq 0$ $\psi_1 \neq 0$ $\psi_2 = 0$ $2\psi_3 = \psi_1 + \partial_y \theta_0$	$\theta_0 \neq 0$ $\theta_1 = 0$ $\theta_2 = 0$ $\theta_3 = 0$
current	S_0,S_1 A_0,A_1 SH_0,SH_1	$\phi_0 \neq 0$ $\phi_1 \neq 0$ $2\phi_2 = a^2 \partial_x \theta_1$ $2\phi_3 = \phi_1 + \partial_x \theta_0$	$\psi_0 \neq 0$ $\psi_1 \neq 0$ $2\psi_2 = a^2 \partial_y \theta_1$ $2\psi_3 = \psi_1 + \partial_y \theta_0$	$\theta_0 \neq 0$ $\theta_1 \neq 0$ $2\theta_2 = a^2 \frac{\lambda}{\lambda+2\mu}(\partial_x \phi_1 + \partial_y \psi_1)$ $2\theta_3 = \theta_1 + \frac{\lambda}{\lambda+2\mu}(\partial_x \phi_0 + \partial_y \psi_0)$

It should be mentioned here that in practical applications concerned with dynamics and wave propagation analysis of shell-like structures the frequencies of excitation signals usually remain much lower than the first cut-off frequency f_1 avoiding in this way the simultaneous excitation of various modes that are very different in their nature in terms of their amplitudes, dispersion characteristics and damping. It can be said that within this range of frequencies the current higher order shell theory under consideration is characterised by the smallest values of the modelling error δ simultaneously for the symmetric and anti-symmetric dynamic behaviour. This plays a significant and very important role in the case of wave propagation analysis when coupled interaction and conversion between symmetric and anti-symmetric modes takes place.

2.4. Time-domain Spectral Finite Element Method

TD-SFEM, as originally proposed by Patera in [17], is based on specific distributions of nodes within SFEs that are different from those known from the classical FEM approach. Thanks to this TD-SFEM has certain unique properties. Typically two different kinds of node distributions are employed by TD-SFEM, these being: Lobatto or Chebyshev node distributions [12, 23]. They are based on the roots of appropriate Lobatto $L_n(x)$ or Chebyshev $U_n(x)$ orthogonal polynomials [12], where $x \in [-1, +1]$.

Thanks to the orthogonality of these polynomials, the discretisation error ϵ associated with the use of TD-SFEM decreases exponentially as a function of their order n with no oscillation effects from the so-called Runge phenomenon [30]. Additionally the application of dedicated discrete integration rules, taking advantage of their orthogonality [12], results in diagonal or almost diagonal and very sparse forms of the characteristic elemental inertia matrices $[\boldsymbol{M}]$, corresponding to the Lobatto or Chebyshev node distributions, respectively. The above mentioned properties make TD-SFEM a very attractive tool everywhere, where high accuracy at minimised computational costs are required, especially in the case of applications concerned with dynamics as well as wave propagation problems.

In the current formulation of the higher order transversely deformable shell SFE the Lobatto node distribution was used based on the 6-th order complete Lobatto polynomial $L_6^c(x)$ [12, 23]. In the normalised

(curvilinear) coordinate system $\xi\eta\zeta$ of the element the coordinates of the element nodes $\xi_i (i = 1, \ldots, 6)$ and $\eta_j (j = 1, \ldots, 6)$ are assumed as the roots of:

$$\begin{array}{l} L_6^c(\xi_i) = 0, \quad i = 1, \ldots, 6 \\ L_6^c(\eta_j) = 0, \quad j = 1, \ldots, 6 \end{array} \tag{9}$$

where the complete Lobatto polynomial $L_6^c(x)$ is defined in the following manner [23]:

$$L_6^c(x) = (1 - x^2) L_4(x) = (1 - x^2) P_5'(x) \tag{10}$$

where $L_4(x)$ is the 4-th order Lobatto polynomial, $P_5(x)$ is the 5-th order Legendre polynomial and the symbol $'$ denotes differentiation in respect of x. The roots $r_i (i = 1, \ldots, 6)$ of the complete Lobatto polynomial $L_6^c(x)$ can be found as:

$$r_i = \pm 1, \pm\sqrt{\frac{1}{3} + \frac{2}{3\sqrt{7}}}, \pm\sqrt{\frac{1}{3} - \frac{2}{3\sqrt{7}}} \tag{11}$$

Two Lagrange interpolation polynomials $p(\xi)$ and $q(\eta)$ can be uniquely built on the specified element nodes $\xi_i (i = 0, \ldots, 6)$ and $\eta_j (j = 0, \ldots, 6)$ as:

$$p(\xi) = \sum_{i=1}^{6} N_i(\xi) p_i, \quad q(\eta) = \sum_{j=1}^{6} N_j(\eta) q_j \tag{12}$$

where $N_i(\xi) (i = 1, \ldots, 6)$ and $N_j(\eta) (j = 1, \ldots, 6)$ are one-dimensional shape functions of the element, while $p_i (i = 1, \ldots, 6)$ and $q_j (j = 1, \ldots, 6)$ represent nodal values of the functions $q(\xi)$ and $p(\eta)$. It should be strongly emphasised at this place that both shape functions $N_i(\xi) (i = 1, \ldots, 6)$ and $N_j(\eta) (j = 1, \ldots, 6)$ are orthogonal in a discrete sense:

$$\int_{-1}^{+1} N_i(x) N_j(x) \underset{\cdot}{\mathrm{x}} = \sum_{k=1}^{6} w_k N_i(x_k) N_j(x_k) = w_i \delta_{ij} \tag{13}$$

where $w_k (k = 1, \ldots, 6)$ are the Gauss-Lobatto-Legendre (GLL) weights and δ_{ij} is the Kronecker symbol [12].

Finally a set of two-dimensional shape functions $\tilde{N}_k(\xi, \eta) (k = 1, \ldots, 36)$ can be constructed by simple multiplication of the one-dimensional shape functions $N_i(\xi) (i = 1, \ldots, 6)$ and $N_j(\eta) (j = 1, \ldots, 6)$ in the following manner:

$$\tilde{N}_k(\xi, \eta) \equiv N_i(\xi) N_j(\eta), \quad k = 1, \ldots, 36, \quad i, j = 1, \ldots, 6 \tag{14}$$

where the index mapping noted by $k = k(i, j)$ depends on a chosen node numbering convention [12, 21–23].

Assuming that the shell element under consideration has a uniform thickness h its geometry can be described in the global coordinate system XYZ by well-known relations from the classical FEM approach [22]. These relationships link, through the element shape functions $\tilde{N}_k (k = 1, \ldots, 36)$, coordinates of any point within the shell element $\{\boldsymbol{X}\} = \{X, Y, Z\}^t$ with the vector of nodal coordinates $\{\boldsymbol{X}_k\} (k = 1, \ldots, 36)$ as well as the unit vector $\{\boldsymbol{V}_{3k}\} (k = 1, \ldots, 36)$ normal to the mid-plane of the element:

$$\begin{array}{c} \{\boldsymbol{X}\} = \sum_{k=1}^{36} \tilde{N}_k(\xi, \eta) \left[\{\boldsymbol{X}_k\} + a\zeta \{\boldsymbol{V}_{3k}\}\right] \\ \{\boldsymbol{X}_k\} = \{X_k, Y_k, Z_k\}^t, \quad \{\boldsymbol{V}_{3k}\} = \{U_{3k}, V_{3k}, W_{3k}\}^t \end{array} \tag{15}$$

where the vectors $\{\boldsymbol{X}_k\} (k = 1, \ldots, 36)$ and $\{\boldsymbol{V}_{3k}\} (k = 1, \ldots, 36)$ are defined at the mid-plane of the element. It can be seen that Eqs. (15) result in the shell element having as many as 36 nodes and 216 degrees of freedom.

Since the displacement field given by Eqs. (1) is defined in the local coordinate system xyz it is necessary to transform these relationships to the global coordinate system XYZ in order to evaluate the elemental characteristic inertia $[\boldsymbol{M}]$ and stiffness $[\boldsymbol{K}]$ matrices. This is a standard and well-known procedure of FEM [22] and it was also used in the case of the current shell element. It is briefly explained below.

The most important aspect of this procedure involves the calculation of the matrix $[\boldsymbol{\Theta}_k](k = 1, \ldots, 36)$ representing local directional cosines associated with element nodes. It should be noted here that in the case of the Lobatto node distribution the local coordinates $\xi_i(i = 1, \ldots, 6)$ and $\eta_j(i = 1, \ldots, 6)$ of element nodes coincide with the coordinates of the abscissas used for numerical evaluation of the inertia $[\boldsymbol{M}]$ and stiffness $[\boldsymbol{K}]$ matrices [12, 23]. The matrix $[\boldsymbol{\Theta}_k](k = 1, \ldots, 36)$ is required to transform all local derivatives associated with the higher order terms of the displacement field $\phi(i = 2, 3)$, $\psi(i = 2, 3)$ and $\theta(i = 2, 3)$, given by Eqs. (2) and Eqs. (3) as well as all components of local strains. It is defined as [22]:

$$[\boldsymbol{\Theta}_k] = [\boldsymbol{V}_{1k}, \boldsymbol{V}_{2k}, \boldsymbol{V}_{3k}], \quad k = 1, \ldots, 36 \tag{16}$$

where $\{\boldsymbol{V}_{1k}\}(k = 1, \ldots, 36)$ and $\{\boldsymbol{V}_{2k}\}(k = 1, \ldots, 36)$ represent two orthonormal vectors defined at the mid-plane of the element and normal to the vector $\{\boldsymbol{V}_{3k}\}(k = 1, \ldots, 36)$.

Based on that definition it can be found that [22]:

$$[\boldsymbol{\epsilon}_k] = [\boldsymbol{\Theta}_k]^t [\boldsymbol{J}_k]^{-1} [\boldsymbol{e}_k] [\boldsymbol{\Theta}_k] \tag{17}$$

with $[\boldsymbol{\epsilon}_k](k = 1, \ldots, 36)$ being the matrix of derivatives defined in the local coordinate systems xyz:

$$[\boldsymbol{\epsilon}_k] = \begin{bmatrix} \partial_x u & \partial_x v & \partial_x w \\ \partial_y u & \partial_y v & \partial_y w \\ \partial_z u & \partial_z v & \partial_z w \end{bmatrix}_k, \quad k = 1, \ldots, 36 \tag{18}$$

where $[\boldsymbol{J}_k](k = 1, \ldots, 36)$ denotes the Jacobian matrix [12, 21–23] mapping the volume of the shell element from the global coordinate system XYZ to the normalised (curvilinear) coordinate system $\xi\eta\zeta$:

$$[\boldsymbol{J}_k] = \begin{bmatrix} \partial_\xi X & \partial_\xi Y & \partial_\xi Z \\ \partial_\eta X & \partial_\eta Y & \partial_\eta Z \\ \partial_\zeta X & \partial_\zeta Y & \partial_\zeta Z \end{bmatrix}_k, \quad k = 1, \ldots, 36 \tag{19}$$

while $[\boldsymbol{e}_k](k = 1, \ldots, 36)$ is the matrix of corresponding derivatives defined also in the normalised (curvilinear) coordinate system $\xi\eta\zeta$ of the element:

$$[\boldsymbol{e}_k] = \begin{bmatrix} \partial_\xi U & \partial_\xi V & \partial_\xi W \\ \partial_\eta U & \partial_\eta V & \partial_\eta W \\ \partial_\zeta U & \partial_\zeta V & \partial_\zeta W \end{bmatrix}_k, \quad k = 1, \ldots, 36 \tag{20}$$

It should be emphasised that in exactly the same manner all higher order derivatives can be evaluated that are associated with all higher order terms of the displacement field $\phi(i = 2, 3)$, $\psi(i = 2, 3)$ and $\theta(i = 2, 3)$ given by Eqs. (2) and Eqs. (3). Then the elemental characteristic inertia $[\boldsymbol{M}]$ and stiffness $[\boldsymbol{K}]$ matrices can be easily calculated based on the standard and well-known procedures common for FEM and TD-SDEM [12, 21–23].

3. Numerical simulations

Results of numerical simulations presented below concern two different types of analysis as well as two different structures. The first structure is a thin-walled spherical shell, representing a pressure vessel, while the second structure is a thin-walled half-pipe structure. It was assumed that in both these cases the structures are made out of aluminium alloy of the following material properties: Young's modulus $E = 72.7$ GPa, Poisson's ratio $nu = 0.33$, density $\rho = 2700$ kg/m^3.

In the case of the thin-walled spherical shell the numerical calculations concerned the analysis of natural frequencies and modes of vibrations as well as the propagation of elastic waves within the shell. In the case of the second structure, i.e. the thin-walled half-pipe, numerical calculations carried out were focused on the propagation of elastic waves. All numerical calculations were carried out by the use of the higher order transversely deformable shell SFE described above and the application of TD-SFEM in MATLAB environment.

3.1. Natural vibrations

Firstly the analysis of natural frequencies and modes of natural vibrations of a thin-walled aluminium spherical shell was carried out. It was initially assumed that the shell thickness h was 5 mm, while its radius R was 1000 mm. The geometry of the shell under investigation is presented in Fig. 7(a), while its exemplary discretisation by higher order transversely deformable shell SFEs in Fig. 7(b). In this analysis the first 45 natural frequencies and modes of natural vibrations were calculated. The results obtained were compared against known analytical solutions [31], as well as the results obtained through the application of the classical FEM approach and a commercial FEM package.

At this point it is interesting to note that in the case of a perfectly symmetrical and isotropic thin-walled elastic sphere there are two main branches of multiple (degenerated) modes of natural vibrations. The first branch represents purely torsional behaviour, where the radial displacement component u_r vanishes, i.e. $u_r = 0$, while the polar u_ϕ and azimuthal u_θ displacement components remain, i.e. $u_\phi \neq 0$ and $u_\theta \neq 0$. Contrary to that the second branch corresponds to coupled radial-extensional behaviour due to shearing and stretching [31]. These two branches are supplemented by a single purely extensional natural vibration mode, where only the radial displacement component u_r exists, i.e. $u_r \neq 0$, while the polar u_ϕ and azimuthal u_θ displacement components vanish, i.e. $u_\phi = u_\theta = 0$.

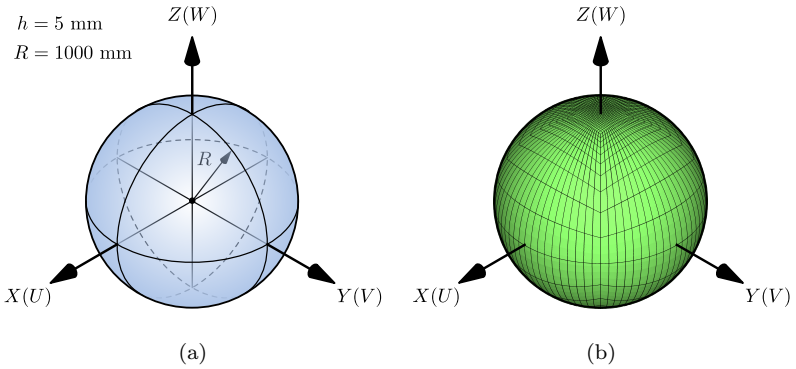

Figure 7: The geometry of a thin-walled spherical shell (a) and its discretisation by 2400 shell SFEs (b) used in the analysis of natural vibrations.

The multiplicity (degeneration degree) of a particular natural frequency (either torsional or coupled) increases linearly [31–33] with the natural frequency number m as $k = 2m + 1$. This is clearly shown in Figs. 8–11. For this reason for a given frequency number m (either torsional or coupled) there exists a set of substantially different modes of natural vibrations (either torsional or coupled), as presented in Fig. 10. As a consequence of this, numerically calculated values of natural frequencies are scattered around a certain average value, which additionally influences the approximation error ϵ by increasing its value. Moreover, due to axisymmetric nature of the primary mode in each set of k multiple (degenerated) modes of natural vibrations, the meshes of SFEs used in this analysis were arranged in such a manner as to expose that symmetry, as presented in Fig. 7(b). The first six axisymmetric modes of natural vibrations calculated numerically by the use of the current formulation of the shell SFE are presented in Fig. 12.

The analysis was carried out for various mesh densities $d_i (i = 1, \ldots, 6)$ in order to show how the discretisation error ϵ influences the results obtained. The mesh densities $d_i (i = 1, \ldots, 6)$ were chosen in such a manner that $S \cdot d_i (i = 1, \ldots, 6)$ was equal to 6, 24, 54, 96, 150 as well as 2400 elements, where S denotes

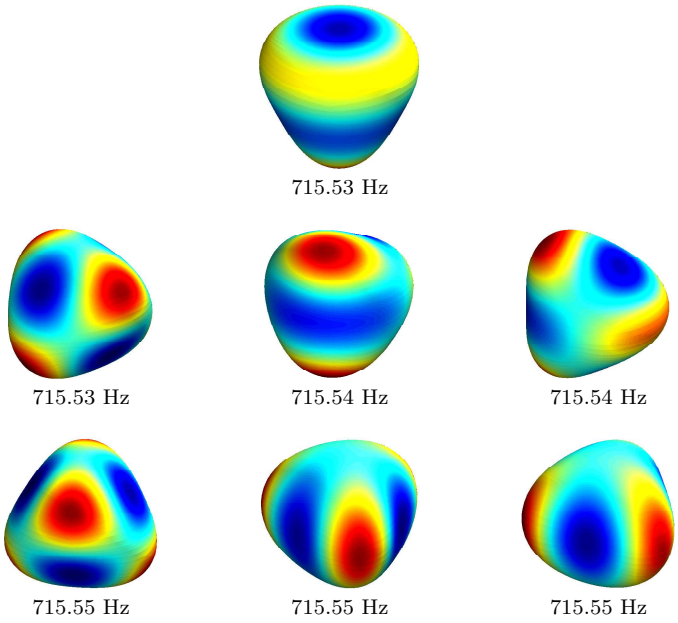

Figure 8: Multiple (degenerated) modes of natural vibrations for the frequency number $m = 3$ calculated for a 5 mm thick isotropic spherical shell based on the use of the current shell SFE for a mesh density $S \cdot d_6 = 2400(60002)$ elements(nodes).

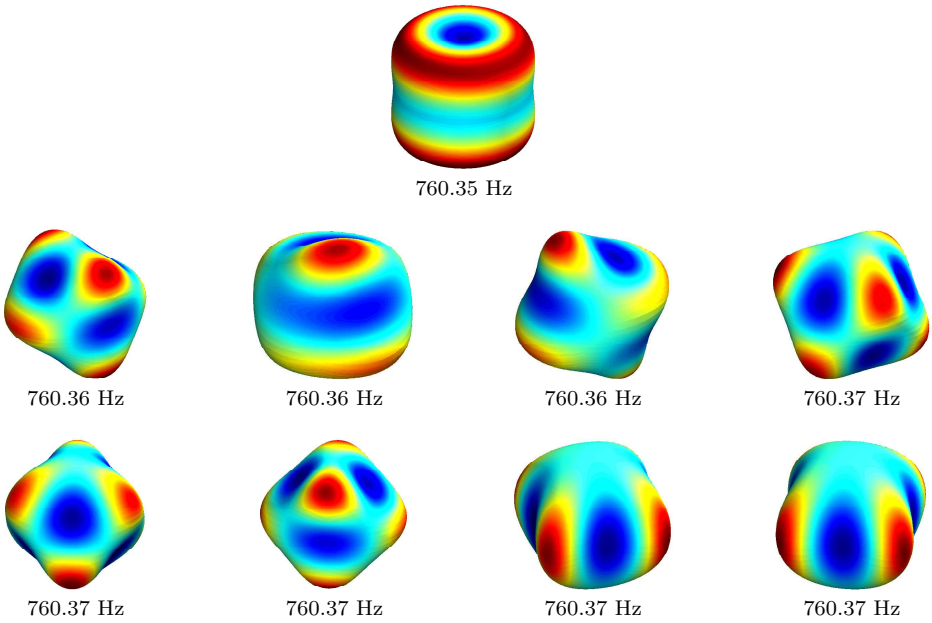

Figure 9: Multiple (degenerated) modes of natural vibrations for the frequency number $m = 4$ calculated for a 5 mm thick isotropic spherical shell based on the use of the current shell SFE for a mesh density $S \cdot d_6 = 2400(60002)$ elements(nodes).

the surface of the spherical shell. Due to the mode multiplicity, apart from the average discretisation error ϵ_m related to a given frequency number m, an additional characteristic of the results obtained was taken into account. It was defined in a similar manner as the standard deviation σ_m of the natural frequencies calculated numerically and related to the exact analytical solution, rather than to the mean value of computational results. For that reason both the average discretisation error ϵ_m as well as the standard deviation σ_m were defined as follows:

$$\epsilon_m = \frac{1}{k}\sum_{i=1}^{k}\epsilon_{m,i}, \quad \epsilon_{m,i} = \frac{f^c_{m,i} - f^a_m}{f^a_m} \times 100\%, \quad m = 2,3,\ldots, \quad k = 1,2,\ldots,2m+1 \tag{21}$$

$$\sigma_m = \sqrt{\frac{1}{k}\sum_{i=1}^{k}\left(f^c_{m,i} - f^a_m\right)^2}, \quad m = 2,3,\ldots, \quad k = 1,2,\ldots,2m+1 \tag{22}$$

where $f^c_{m,i}$ denotes the i-th natural frequency calculated numerically and associated with the i-th mode of natural vibration out of k multiple (degenerated) modes belonging to the frequency number m, while f^a_m is the value of the same natural frequency calculated analytically [31].

The results obtained by the application of the shell SFE under investigation are presented in Tab. 2 as the natural frequency relative error ϵ_m and standard deviation σ_m calculated on the basis of the current shell SFE for a 5 mm thick spherical shell as a function of mesh density. It can be seen from the results presented in Tab. 2 that the current formulation of the shell SFE can be characterised by extremely good accuracy for all mesh densities considered except d_1. In this case higher values of the natural frequency relative error ϵ_m as well as the natural frequency standard deviation σ_m results from wrong estimation of the multiplicity k of particular natural frequencies m.

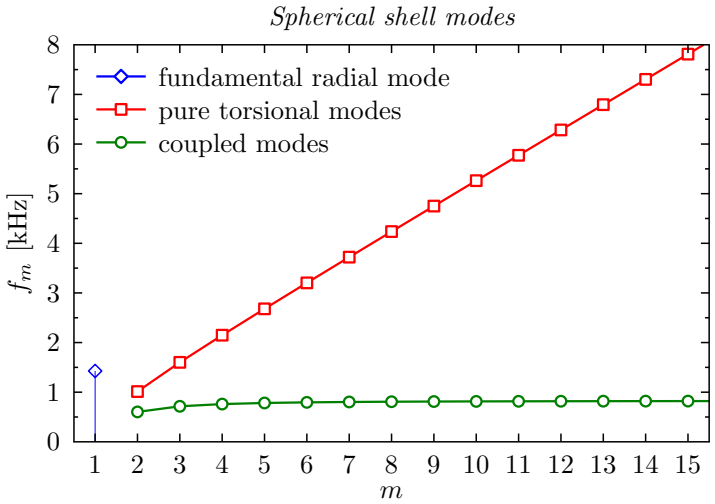

Figure 10: Natural frequencies of a thin-walled elastic, isotropic spherical shell.

In order to compare the results of numerical calculations obtained by the application of the current higher order transversely deformable shell SFE a comparative analysis was performed, for which a commercial FEM package was employed. The results of this analysis are presented in Tab. 3 and were obtained by the use of the Autodesk TYPE-6 triangle shell FEs [21, 22]. In this analysis the total number of degrees of freedom of numerical models used were kept close to, or in favour of, the commercial FEM package.

It can be found that the values of the average discretisation error ϵ_m, calculated in the case of the results obtained by the commercial FEM package, are comparable with the current shell SFE with slightly higher values. However, this is not the case with the standard deviation σ_m of the calculated natural frequency. Their values indicate a high dispersion of the natural frequency associated with a given frequency number

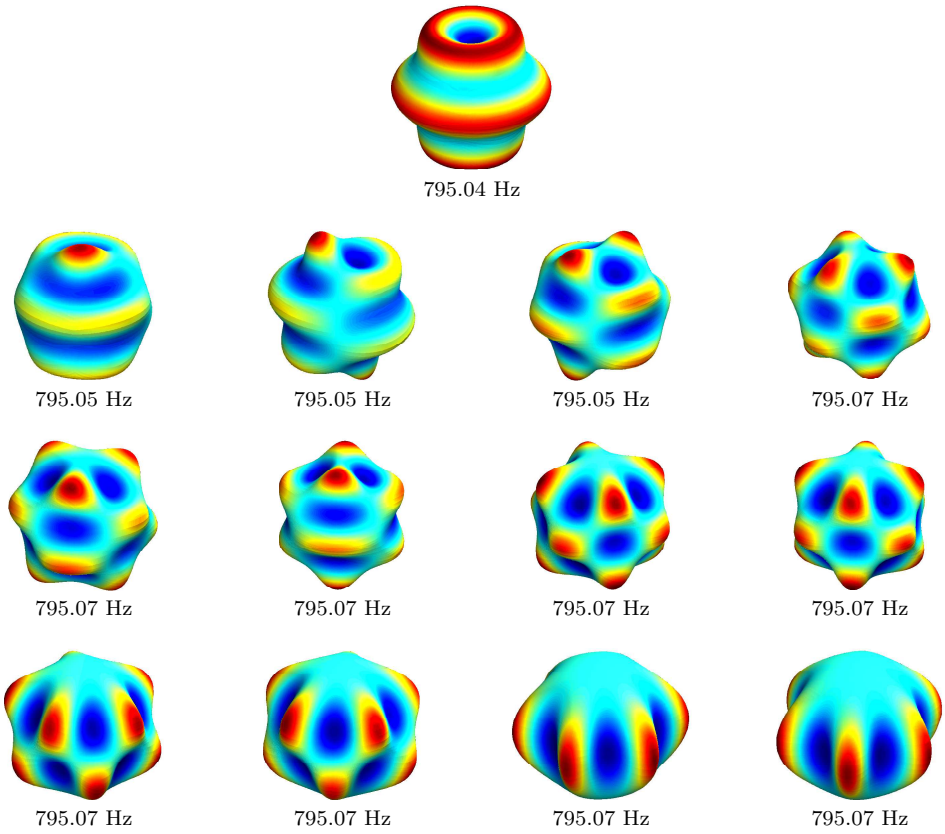

Figure 11: Multiple (degenerated) modes of natural vibrations for the frequency number $m = 6$ calculated for a 5 mm thick isotropic spherical shell based on the use of the current shell SFE for a mesh density $S \cdot d_6 = 2400(60002)$ elements(nodes).

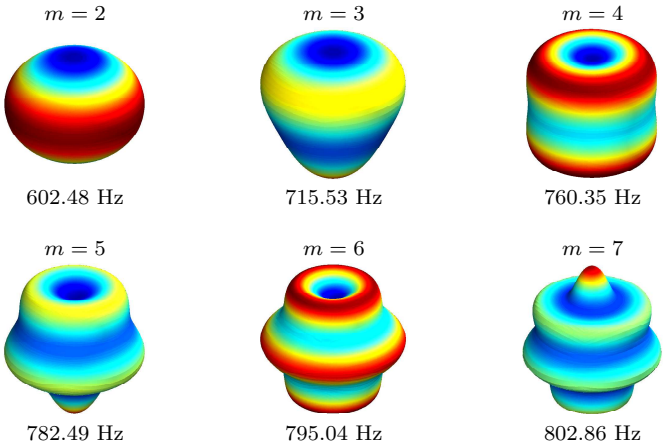

Figure 12: First six axisymmetric modes of natural vibrations calculated for a 5 mm thick isotropic spherical shell based on the use of the current shell SFE for a mesh density $S \cdot d_6 = 2400(60002)$ elements(nodes).

m, which increases rapidly with the frequency number m and which reaches considerable values for smaller mesh densities. For example, the value of the average discretisation error ϵ_4 is -0.67% and the value of the standard deviation σ_4 is 12.4 Hz for the mesh density $S \cdot d_2$. In contrast, the corresponding values of the average discretisation error ϵ_4 and standard deviation σ_4, obtained for the current formulation of the shell SFE, are 0.0% and 0.01 Hz.

Table 2: Natural frequency relative error ϵ_m and standard deviation σ_m calculated for a 5 mm thick isotropic spherical shell based on the use of the current shell SFE for selected mesh densities: $S \cdot d_1 = 6(152)$, $S \cdot d_2 = 24(602)$, $S \cdot d_3 = 54(1352)$, $S \cdot d_4 = 96(2402)$, $S \cdot d_5 = 150(3752)$, $S \cdot d_6 = 2400(60002)$ elements(nodes).

Mode number	Mode multiplicity			ϵ_m			
m	k	d_1	d_2	d_3	d_4	d_5	d_6
2	5	0.00%	0.00%	0.00%	0.00%	0.00%	0.00%
3	7	–0.01%	0.00%	0.00%	0.00%	0.00%	0.00%
4	9	–1.47%	0.00%	0.00%	0.00%	0.00%	0.00%
5	11	–1.79%	0.00%	0.00%	0.00%	0.00%	0.00%
6	13	–1.45%	0.00%	0.00%	0.00%	0.00%	0.00%
Mode number	Mode multiplicity			σ_m			
m	k	d_1	d_2	d_3	d_4	d_5	d_6
2	5	0.01 Hz	0.00 Hz	0.00 Hz	0.00 Hz	0.00 Hz	0.00 Hz
3	7	0.14 Hz	0.00 Hz	0.00 Hz	0.00 Hz	0.01 Hz	0.01 Hz
4	9	18.93 Hz	0.01 Hz	0.01 Hz	0.01 Hz	0.01 Hz	0.01 Hz
5	11	15.97 Hz	0.02 Hz	0.02 Hz	0.02 Hz	0.02 Hz	0.02 Hz
6	13	11.96 Hz	0.07 Hz	0.03 Hz	0.03 Hz	0.03 Hz	0.03 Hz

Table 3: Natural frequency relative error ϵ_m and standard deviation σ_m calculated for a 5 mm thick isotropic spherical shell based on the use of the Autodesk TYPE-6 triangle shell FE for selected mesh densities: $S \cdot d_1 = 296(150)$, $S \cdot d_2 = 1200(602)$, $S \cdot d_3 = 2992(1498)$, $S \cdot d_4 = 5080(2542)$, $S \cdot d_5 = 7776(3890)$, $S \cdot d_6 = 134944(67474)$ elements(nodes).

Mode number	Mode multiplicity			ϵ_m			
m	k	d_1	d_2	d_3	d_4	d_5	d_6
2	5	0.55%	0.31%	0.13%	0.08%	0.06%	0.01%
3	7	–2.44%	0.32%	0.22%	0.16%	0.11%	0.01%
4	9	–2.38%	–0.67%	0.30%	0.25%	0.17%	0.02%
5	11	–1.46%	0.01%	0.38%	0.34%	0.24%	0.03%
6	13	1.63%	1.23%	0.39%	0.44%	0.31%	0.04%
Mode number	Mode multiplicity			σ_m			
m	k	d_1	d_2	d_3	d_4	d_5	d_6
2	5	6.57 Hz	2.38 Hz	0.85 Hz	0.51 Hz	0.36 Hz	0.03 Hz
3	7	25.24 Hz	8.45 Hz	2.13 Hz	1.25 Hz	0.85 Hz	0.09 Hz
4	9	19.59 Hz	12.40 Hz	3.69 Hz	2.08 Hz	1.38 Hz	0.17 Hz
5	11	14.96 Hz	9.23 Hz	4.67 Hz	2.89 Hz	1.97 Hz	0.24 Hz
6	13	17.10 Hz	10.83 Hz	4.63 Hz	3.98 Hz	2.81 Hz	0.34 Hz

In a similar manner as above the influence of the relative thickness h/R of the spherical shell under investigation was taken into account. It was assumed in this analysis that the thickness h of the spherical shell could vary, while its radius R was constant. Different values of the shell thickness $h_i (i = 1, \ldots, 6)$ were considered equal to 1 mm, 2 mm, 10 mm, 15 mm, 20 mm as well as 25 mm. This analysis was carried out for the mesh density $S \cdot d_3$. The results of numerical calculations obtained on the basis of the current formulation of the higher order transversely deformable shell SFE are presented in Tab. 4, while those corresponding to the application of the commercial FEM package are presented in Tab. 5. Also in this case the same observations can be made.

In the whole range of the relative thickness h/R considered as well as the modes of natural vibrations the results of numerical calculations obtained by the use of the current higher order transversely deformable shell SFE can be characterised by very small values of the average discretisation error ϵ_m. This error reaches its extreme value of -0.12% in the worst case, i.e. the shell thickness h_6 equal to 0.025 mm and the frequency number m equal to 6. Similarly, the standard deviation of natural frequencies σ_m stays very small and reaches its maximum value of 1.01 Hz for the same shell thickness h_6 and the frequency number m. It is

interesting to note that in the present analysis the values of both the average discretisation error ϵ_m and the natural frequency standard deviation σ_m increase towards higher values of the relative thickness h/R as well as towards higher frequency numbers m characterised by greater multiplicity (higher degeneration) of the associated modes of natural vibrations.

Table 4: Natural frequency relative error ϵ_m and standard deviation σ_m calculated for an isotropic spherical shell and the mesh density d_3 based on the use of the current shell SFE for selected values of relative thickness h/R: $h_1 = 0.001$, $h_2 = 0.005$, $h_3 = 0.010$, $h_4 = 0.015$, $h_5 = 0.020$, $h_6 = 0.025$ mm.

Mode number	Mode multiplicity			ϵ_m			
m	k	h_1	h_2	h_3	h_4	h_5	h_6
2	5	0.00%	0.00%	0.00%	0.00%	–0.01%	–0.02%
3	7	0.00%	0.00%	0.00%	–0.01%	–0.02%	–0.04%
4	9	0.00%	0.00%	–0.01%	–0.02%	–0.03%	–0.06%
5	11	0.00%	0.00%	–0.01%	–0.03%	–0.05%	–0.09%
6	13	0.00%	0.00%	–0.01%	–0.03%	–0.07%	–0.12%
Mode number	Mode multiplicity			σ_m			
m	k	h_1	h_2	h_3	h_4	h_5	h_6
2	5	0.00 Hz	0.00 Hz	0.00 Hz	0.01 Hz	0.04 Hz	0.13 Hz
3	7	0.00 Hz	0.00 Hz	0.02 Hz	0.06 Hz	0.13 Hz	0.29 Hz
4	9	0.00 Hz	0.01 Hz	0.05 Hz	0.12 Hz	0.25 Hz	0.51 Hz
5	11	0.00 Hz	0.02 Hz	0.08 Hz	0.21 Hz	0.40 Hz	0.75 Hz
6	13	0.00 Hz	0.03 Hz	0.11 Hz	0.28 Hz	0.54 Hz	1.01 Hz

Table 5: Natural frequency relative error ϵ_m and standard deviation σ_m calculated for an isotropic spherical shell calculated and the mesh density d_3 based on the use of the Autodesk TYPE-6 triangle shell FE for selected values of relative thickness t/R: $h_1 = 0.001$, $h_2 = 0.005$, $h_3 = 0.010$, $h_4 = 0.015$, $h_5 = 0.020$, $h_6 = 0.025$ mm.

Mode number	Mode multiplicity			σ_m			
m	k	h_1	h_2	h_3	h_4	h_5	h_6
2	5	0.00%	0.13%	0.16%	0.18%	0.19%	0.20%
3	7	–0.61%	0.22%	0.32%	0.36%	0.39%	0.41%
4	9	–3.92%	0.30%	0.50%	0.57%	0.62%	0.66%
5	11	5.28%	0.38%	0.73%	0.84%	0.91%	0.97%
6	13	–4.17%	0.39%	0.99%	1.16%	1.25%	1.34%
Mode number	Mode multiplicity			σ_m			
m	k	h_1	h_2	h_3	h_4	h_5	h_6
2	5	0.34 Hz	0.85 Hz	1.07 Hz	1.16 Hz	1.24 Hz	1.32 Hz
3	7	5.08 Hz	2.13 Hz	2.74 Hz	2.97 Hz	3.13 Hz	3.28 Hz
4	9	30.23 Hz	3.69 Hz	4.55 Hz	4.98 Hz	5.29 Hz	5.59 Hz
5	11	41.37 Hz	4.67 Hz	6.55 Hz	7.31 Hz	7.86 Hz	8.37 Hz
6	13	33.99 Hz	4.63 Hz	8.74 Hz	10.17 Hz	10.97 Hz	11.78 Hz

This is not the case for the results of numerical calculations obtained by the use of the commercial Autodesk FEM package and the application of TYPE-6 triangle shell FEs. It can be clearly seen from Tab. 5 that the corresponding values of the average discretisation error ϵ_m and the natural frequency standard deviation σ_m are much higher and they tend to their extreme values not only in the case of higher frequency numbers m, but also in the case of very thin and thick shell FEs used, i.e. for the shell thickness h_1 equal to 1 mm and h_6 equal to 0.025 mm. For example, the value of the average discretisation error ϵ_5 is 5.28% and the value of the standard deviation σ_5 is 41.37 Hz for the shell thickness h_1. In contrast, the corresponding values of the average discretisation error ϵ_5 and standard deviation σ_5, obtained for the current formulation of the shell SFE, are 0.0% and 0.0 Hz.

3.2. Wave propagation

Secondly the analysis of wave propagation in the same thin-walled aluminium spherical shell was carried out. It was assumed for that analysis that the shell thickness h and its radius R remained the same. The geometry of the shell under investigation is presented in Fig. 13(a), while its discretisation by higher order transversely deformable shell SFEs in Fig. 13(b). It should be mentioned here that discretisation

requirements for this type of analysis are different. The analysis of wave propagation requires uniform, or close to uniform, discretisation by a mesh of SFEs since strong irregularities in the mesh density results in so-called mesh anisotropy [12]. A direct consequence of this anisotropy are different wave propagation velocities in different spatial directions x, y and z, which effect should be avoided as it leads to significant numerical errors. In the current analysis it was additionally assumed that the spherical shell under investigation was

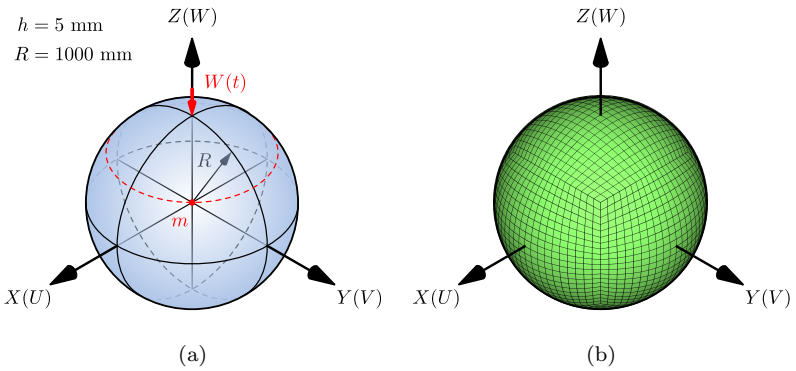

Figure 13: The geometry of a thin-walled spherical shell (a) and its discretisation by 2400 shell SFEs (b) used in the analysis of wave propagation.

excited kinematically by a transverse displacement component $W(t)$ acting on the top surface of the spherical shell, as shown in Fig. 13(a). The amplitude of this excitation was 100 μm and it had a form of 5 sine pulses modulated by the Hann window. The carrier frequency f_c was 5 kHz, while the modulation frequency f_m was 1 kHz. The excitation signal in both time and frequency domains are presented in Fig. 14.

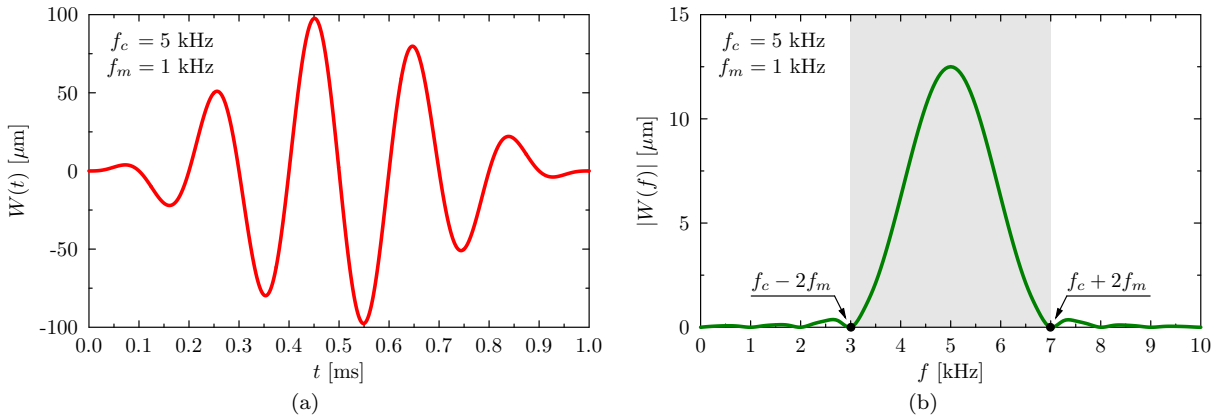

Figure 14: Excitation signal in the time domain (a) and in the frequency domain (b).

Apart from that an additional mass m was located on the top surface of the spherical shell at the polar ϕ and azimuthal θ angles equal to 45° and equal to 0.001 of the total mass of the structure. Wave propagation patterns were observed over the total time span of 4 ms, which was divided into 16,000 equal time steps. As a solution to the equation of motion the method of central difference was chosen. No material or numerical damping was assumed.

The results obtained by the application of the current formulation of the higher order transversely deformable shell SFE are presented in Fig. 15 at different time instances. It should be added that due to the curvature of the shell surface wave propagation patterns are displayed as representing the total displacement magnitude defined as $\sqrt{U^2 + V^2 + W^2}$, where U, V and W are the displacement components defined in the global coordinate system XYZ.

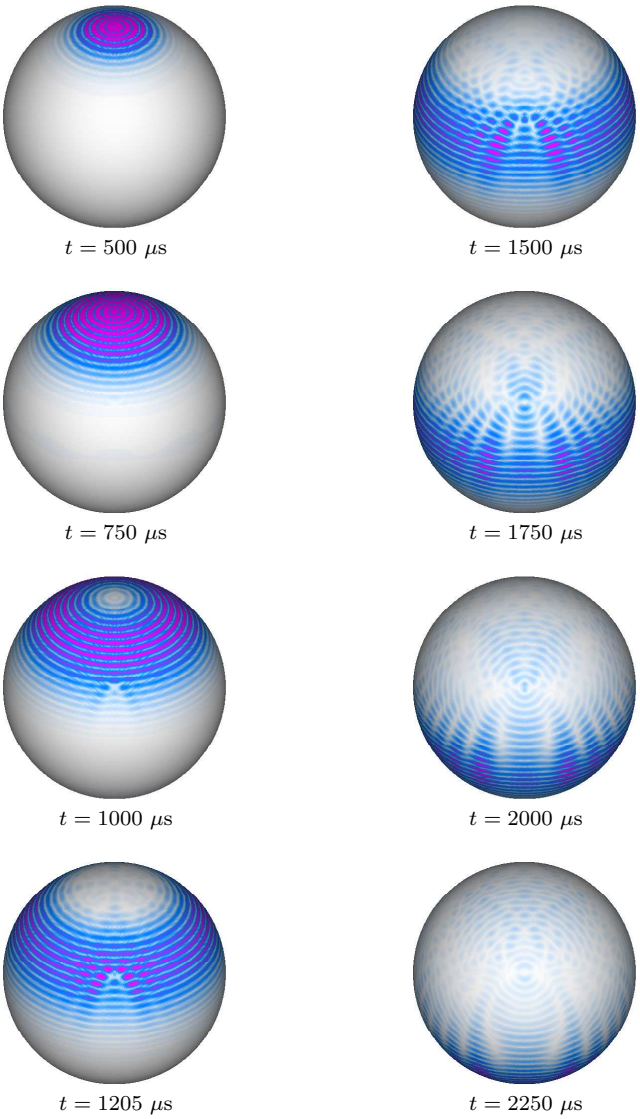

Figure 15: Wave propagation patterns for coupled S_0, SH_0 and A_0 wave propagation modes at various time instances, for a 5 mm thick isotropic spherical shell with an additional mass, based on the use of TD-SFEM and current shell SFE for a mesh density $S \cdot d_6 = 2400(60002)$ elements(nodes).

Due to the selected excitation frequency of 5 kHz three wave propagation modes are allowed to propagate within the spherical shell, these being: two symmetric (*membrane*) modes S_0 and SH_0 as well as one anti-symmetric (*bending*) mode A_0. The symmetric (*membrane*) modes can be assumed as non-dispersive because of relatively small or no difference between their phase c_g and group velocities c_p. In the current case their values are approximately: $c_g = 5.48$ km/s and $c_p = 5.49$ km/s for S_0 mode, $c_g = 3.18$ km/s and $c_p = 3.18$ km/s for SH_0, respectively. However, the anti-symmetric (*bending*) mode is highly dispersive. The corresponding values are approximately $c_g = 2.54$ km/s and $c_p = 1.48$ km/s. An additional source of dispersion of the wave propagation patterns comes from the geometry of the spherical shell, which strongly couples all wave propagation directions. This is clearly shown in the case of the wave propagation patterns associated with time instances t greater that 1500 μs. Moreover, as a consequence of the excitation form the wave propagation patterns observed are dominated by the anti-symmetric (*bending*) mode A_0.

As a final structure a thin-walled aluminium half-pipe was investigated. As before it was assumed for the analysis that the shell thickness h and its radius R remained the same, while the total length L of the half-pipe was 3000 mm. The geometry of the half-pipe under investigation is presented in Fig. 16(a), while its discretisation by higher order transversely deformable shell SFEs is shown in Fig. 16(b).

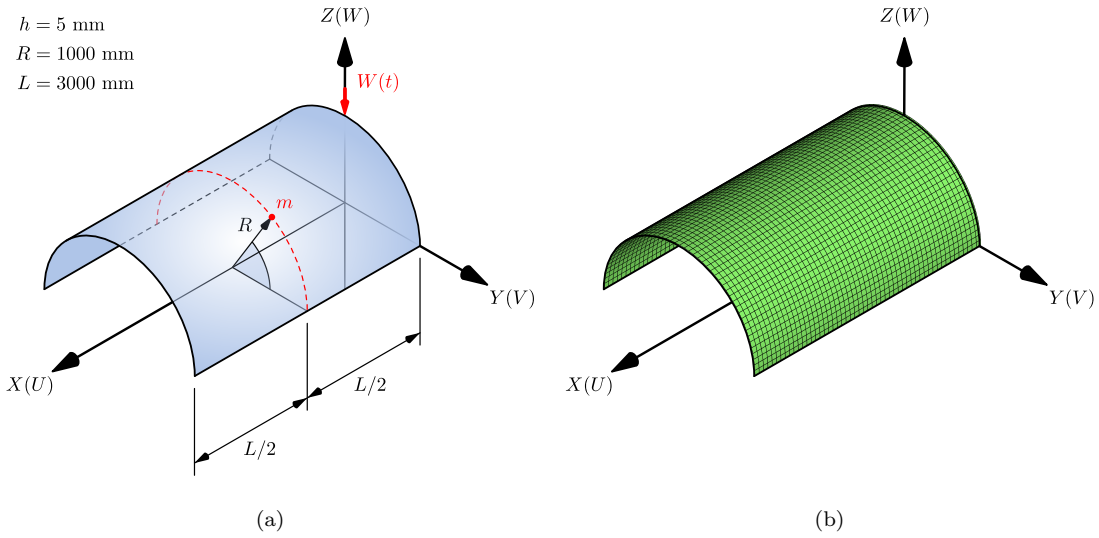

Figure 16: The geometry of a thin-walled half-pipe (a) and its discretisation by 2704 shell SFEs (b) used in the analysis of wave propagation.

In the same manner as previously it was additionally assumed that the half-pipe was excited kinematically by a transverse displacement component $W(t)$ acting on the top surface of the spherical shell, as shown in Fig. 16(a). The amplitude of this excitation was 0.1 mm and it had the same form of 5 sine pulses modulated by the Hann window. Their carrier frequency was also 5 kHz. Also an additional mass m was located at half its length on the top surface of the half-pipe at the polar angle ϕ equal to 45° and equal to 0.001 of the total mass of the structure. Similarly, wave propagation patterns were observed over the total time span of 4 ms, which was divided into 16,000 equal time steps. The same solution to the equation of motion was chosen with no material nor numerical damping.

The results obtained are presented in Fig. 17 as wave propagation patterns at different time instances as representing the total displacement magnitude defined as before as $\sqrt{U^2 + V^2 + W^2}$, where U, V and W are the displacement components defined in the global coordinate system XYZ.

Due to the same type of excitation as well as material properties and the thickness of the structure the same observations can be made also in this case. Selected excitation frequency of 5 kHz results in three wave propagation modes, these being: two symmetric (*membrane*) modes S_0 and SH_0 as well as one anti-symmetric (*bending*) mode A_0 of the same dispersion characteristics.

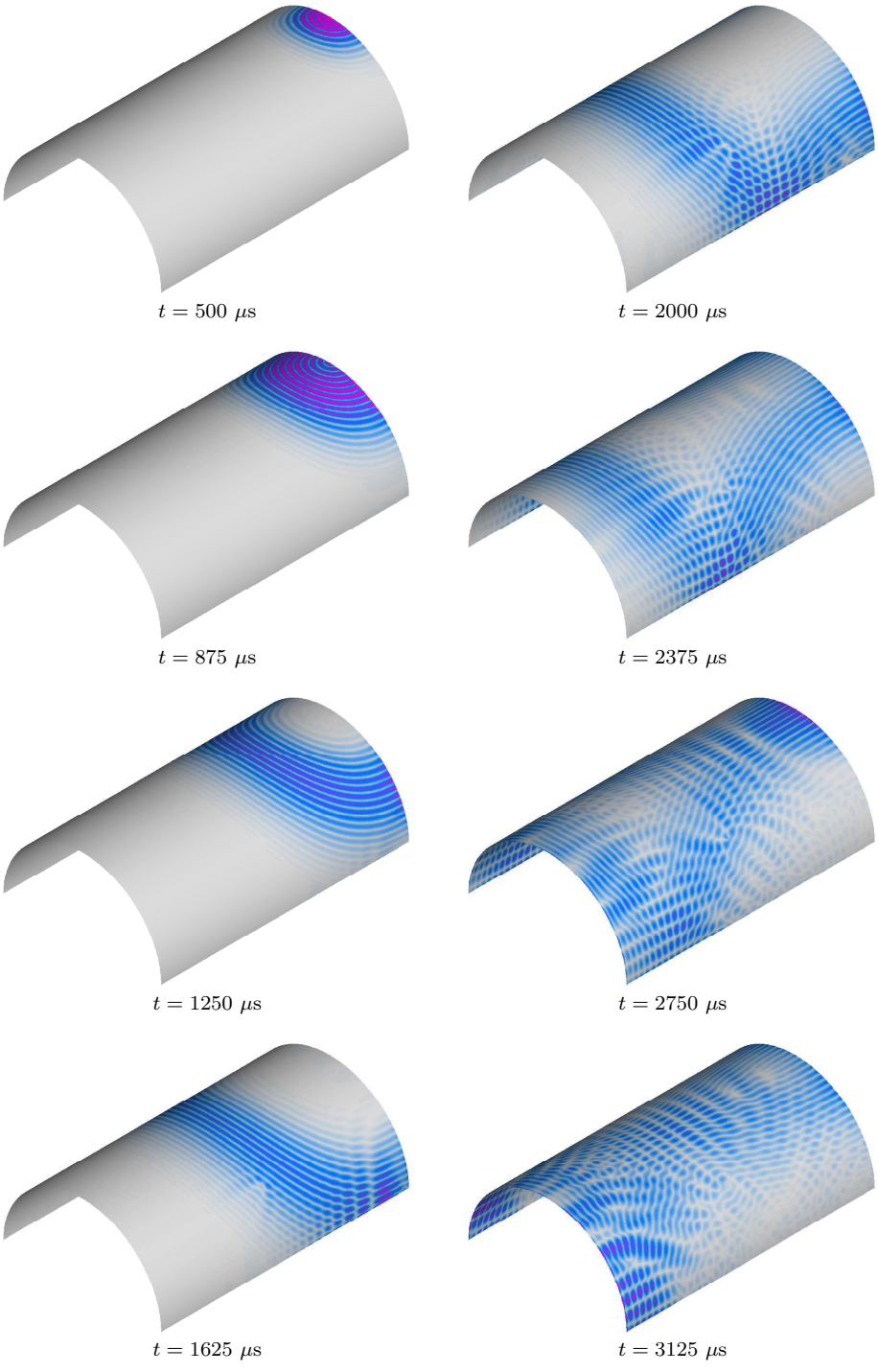

Figure 17: Wave propagation patterns for coupled S_0, SH_0 and A_0 wave propagation modes at various time instances, for a 5 mm thick isotropic half-pipe with an additional mass, based on the use of TD-SFEM and current shell SFE for a mesh density $S \cdot d_6 = 2704(68121)$ elements(nodes).

4. Conclusions

Numerical simulations have become a very important activity in engineering sciences as they are a source of very valuable information about structural behaviour. Therefore it is very important to develop and test more efficient and more sophisticated models that enable their users to gain a deeper insight into simulated phenomena. Dynamic problems, especially those related to the propagation of elastic waves, remain not only very important, but also very demanding due to the complexity of simulated phenomena as well as the geometrical properties of investigated structures. The concept of a higher order transversely deformable shell SFE appears as a very good solution, especially when combined with such an effective numerical tool as TD-SFEM.

The results presented in the current paper allow the authors to draw a number of general conclusions. They can be formulated in the following way:

- The methodology employed by the authors to construct the displacement field of the higher order transversely deformable shell SFE can be thought of as a general and universal approach to generate the displacement fields of other higher order FEs or SFEs based of the assumption of the zero traction boundary conditions for τ_{yz}, τ_{zx} and σ_{zz} stress components on the upper and lower surfaces of the elements.

- Further on, a method to generate the dispersion curves associated with the displacement fields obtained is presented by the authors, which utilises Hamilton's principle and which leads to a set of associated equations of motion. These equations are presented in the paper for the case of the analysed shell SFE as well as the dispersion curves resulting from them.

- Comparison analysis of the dispersion curves shown confirms that the current shell SFE is characterised by higher accuracy than classical shell theories developed by Mindlin or Reddy, which is clearly seen in the case of the fundamental symmetric (*membrane*) and anti-symmetric (*bending*) wave propagation modes.

- TD-SFEM as a numerical computational technique serves as perfect implementation grounds for the application of higher order theories developed not only for the purpose of high frequency dynamics, but also in the case of classical modal analysis or even static problems. This is very clearly presented for modal and wave propagation analysis of the spherical shell.

- Modal analysis of a spherical shell, which by itself presents a serious computational challenge due to the advancing multiplicity (degeneration) of natural vibration modes with an increase in the natural frequency number, proves that the application of the current shell SFE leads to much smaller discretisation errors and their dispersion than typical FEs. It also proves to be less sensitive to the relative shell thickness, which additionally enhances its application fields. However, it must be remembered that this type of analysis is very sensitive to the discretisation of the computational domain. This was easily observed in the case of modal and wave propagation analysis, which required different discretisation of the very same computational domain.

- Combined application of TD-SFEM and the higher order transversely deformable shell SFE developed by the authors helps to reduce significantly modelling and discretisation errors of numerical investigation providing excellent accuracy, especially in comparison to the classical FEM and typical FEs commonly used for that purpose.

- The ability of the current shell SFE to deform transversely is a very desirable feature in the context of its application for wave propagation problems, where the ease of excitation of either symmetric (*membrane*) and/or anti-symmetric (*bending*) wave propagation modes is very important. Additionally, it greatly improves the accuracy of modelling of the symmetric (*membrane*) wave propagation modes, especially the fundamental S_0 mode. In the case of the classical FEM this feature is achievable only through the application of 3-D FEs, which greatly increases computational costs.

5. Acknowledgements

The Authors of this work would like to gratefully acknowledge the support for their research provided by the Academic Computer Centre in Gdansk. All results presented in this paper have been obtained by the use of the software available at the Academic Computer Centre in Gdansk.

References

[1] J. W. S. Rayleigh, The Theory of Sound, Dover Publications, Inc., New York, 1945.
[2] J. D. Achenbach, Wave Propagation in Elastic Solids, North-Holland Publishing Company, Amsterdam, 1973.
[3] J. L. Rose, Ultrasonic Waves in Solid Media, Cambridge University Press, Cambridge, 1999.
[4] J. Zhang, L. Jia, Y. Shu, Wave propagation characteristics of thin shells of revolution by frequency-wave number spectrum method, Journal of Sound and Vibration 251 (2002) 367–372.
[5] F. G. Yuan, C. C. Hsieh, Three-dimensional wave propagation in composite cylindrical shells, Composite Structures 42 (1998) 153–167.
[6] K. M. Liew, Q. Wang, Analysis of wave propagation in carbon nanotubes via elastic shell theories, International Journal of Engineering Science 45 (2007) 227–241.
[7] C. L. Khanh, High frequency vibrations and wave propagation in elastic shells: Variational-asymptotic approach, International Journal of Solids and Structures 34 (1997) 3923–3939.
[8] V. A. Zarutskii, I. Y. Podil'chuk, Propagation of harmonic waves in longitudinally reinforced cylindrical shells with low shear stiffness, International Applied Mechanics 42 (2006) 525–528.
[9] A. Ghoshal, A. Accorsi, L. Michael, M. S. Bennett, Wave propagation in circular cylindrical shells with periodic axial curvature, Wave Motion 23 (1996) 339–352.
[10] C. Liu, F. Li, W. Huang, Transient wave propagation and early short time transient responses of laminated composite cylindrical shells, Composite Structures 93 (2011) 2587–2597.
[11] A. Żak, A novel formulation of a spectral plate element for wave propagation in isotropic structures, Finite Element in Analysis and Design 45 (2009) 650–658.
[12] W. Ostachowicz, P. Kudela, M. Krawczuk, A. Żak, Guided Waves in Structures for SHM. The Time-domain Spectral Element Method, John Wiley & Sons Ltd., Singapore, 2012.
[13] S. A. Rizzi, J. F. Doyle, A spectral element approach to wave motion in layered solids, Journal of Vibration and Acoustics 114 (1992) 569–577.
[14] J. F. Doyle, Wave Propagation in Structures, Springer-Verlag, Inc., New York, 1997.
[15] S. Gopalakrishnan, J. F. Doyle, Spectral super-elements for wave-propagation in structures with local nonuniformities, Computer Methods in Applied Mechanics and Engineering 121 (1995) 79–90.
[16] S. Gopalakrishnan, A. Chakraborty, D. Roy Mahapatra, Spectral finite element method: Wave propagation, diagnostics and control in anisotropic and inhomogeneous structures, Springer-Verlag London, London, 2008.
[17] A. T. Patera, A spectral element method for fluid dynamics: Laminar flow in a channel expansion, Journal of Computational Physics 54 (1984) 468–488.
[18] O. O. Ochoa, J. N. Reddy, Finite Element Analysis of Composite Laminates, Kluwer Academic Publishers, Dordrecht, 1992.
[19] A. Żak, M. Krawczuk, Assessment of rod behaviour theories used in spectral finite element modelling, Journal of Sound and Vibration 329 (2010) 2099–2113.
[20] A. Żak, M. Krawczuk, Assessment of flexural beam behaviour theories used for dynamics and wave propagation problems, Journal of Sound and Vibration 331 (2012) 5715–5731.
[21] S. S. Rao, The Finite Element Method in Engineering, Pergamon Press, Oxford, 1981.
[22] O. C. Zienkiewicz, The Finite Element Method, McGraw-Hill Book Company, London, 1989.
[23] C. Pozdrikidis, Introduction to Finite and Spectral Element Methods using MATLAB, Chapman and Hall//CRC, Boca Raton, 2005.
[24] Z. Su, L. Ye, Y. Lu, Guided lamb waves for identification of damage in composite structures: A review, Journal of Sound and Vibration 295 (2006) 753–780.
[25] V. Giurgiutiu, Structural Health Monitoring with Piezoelectric Wafer Active Sensors, Academic Press, Oxford, 2007.
[26] Z. Su, L. Ye, Identification of Damage using Lamb Waves. From Fundamentals to Applications, Springer-Verlag, London, 2009.
[27] M. Engholm, Ultrasonic arrays for sensing and beamforming of Lamb waves, Acta Universitatis Upsaliensis Uppsala, Uppsala, 2010.
[28] H. Lamb, On waves in an elastic plate, Proceedings of the Royal Society of London 93 (1917) 293–312.
[29] A. E. Love, A Treatise on the Mathematical Theory of Elasticity, Dover Publications, New York, 1944.
[30] J. P. Boyd, Chebyshev and Fourier Spectral Methods, Dover Publications, Inc., New York, 2000.
[31] R. D. Blevins, Formulas for Natural Frequency and Mode Shapes, Krieger Publishing Company, Amsterdam, 1976.
[32] H. Lamb, On the vibrations of an elastic sphere, Proceedings of the London Mathematical Society 13 (1882) 189–212.
[33] T. A. Duffey, J. E. Pepin, A. N. Robertson, S. M. L., K. Coleman, Vibrations of complete spherical shells with imperfections, Journal of Vibration and Acoustics 129 (2007) 1–18.